PAPER
Jun Hyuk Moon *et al.*
Janus architecture host electrode for mitigating lithium-ion
polarization in high-energy-density Li–S full cells

Check for updates

Janus architecture host electrode for mitigating lithium-ion polarization in high-energy-density Li–S full cells†

Kyungsik Um,‡ Chanho Jung,‡ Hyunsuk Nam, Haeli Lee, Saegi Yeom and Jun Hyuk Moon [ID] *

High-energy-density Li–S full cells require thick host electrodes, which are particularly challenged by diffusion-limited Li-ion polarization. Our study introduces a heterogeneous Janus architecture that mitigates this polarization and achieves uniform charge/discharge reaction rates across the electrodes. Janus electrodes are fabricated by incorporating Mo_2C-coated carbon nanotubes (CNTs) or carbon fibers (CFs) with their uncoated counterparts for the cathode and anode, respectively. At the cathode, the Janus film suppresses the polysulfide shuttle by delaying polysulfide diffusion, even under ultra-high S loading of 10 mg cm^{-2}. At the anode, the film uniformly regulates significant Li plating/stripping within the anode substrate, even at an exceptionally high areal capacity of 20 mA h cm^{-2} accompanying the S loading. Equipped with Janus films on both electrodes and operating under practical conditions with an electrolyte-to-sulfur (E/S) ratio of 4.4 μL mg^{-1} and a negative-to-positive (N/P) ratio of 2, our Li–S full cell achieves an energy density of 6.3 mA h cm^{-2}. These findings underscore the critical role of macroscopic control of the host electrode in enhancing performance.

Broader context

Despite advancements in Li–S battery technology, developing practical Li–S batteries with energy densities surpassing those of Li-ion batteries remains challenging. This is primarily due to the need for high sulfur loading (>5 mg cm^{-2}) cathodes. We confirm that high sulfur loading necessitates a cathode substrate thickness of >150–200 μm, leading to significant Li-ion polarization. This polarization causes uneven sulfur conversion across the cathode and leads to rapid dendritic growth at the anode. To address these issues, we present a Janus architecture combining Mo_2C-coated carbon layers with uncoated counterparts for both the cathode and anode. The Janus cathode ensures uniform conversion kinetics, suppressing the polysulfide shuttle. Additionally, the Janus anode mitigates diffusion-limited dendrite formation, achieving stable Li plating and stripping. Under practical conditions with an S loading of 6 mg cm^{-2}, an E/S ratio of 4.4 μL mg^{-1}, and an N/P ratio of 2, the Janus full cell achieves an areal capacity of 6.3 mA h cm^{-2}. This performance surpasses the typical areal capacity of 4 mA h cm^{-2} in conventional Li-ion batteries. Our findings underscore the impact of macroscopic control of the electrode substrate on Li–S battery performance, presenting a new platform for high-energy-density batteries.

The quest for next-generation energy storage materials has led to Li–S batteries as a viable alternative to Li-ion batteries.[1,2] Li–S batteries are attractive due to not only their high theoretical capacity (S: 1675 mA h g^{-1}, Li: 3860 mA h g^{-1}) but also the cost-effectiveness of S.[3,4] However, the practical application of Li–S batteries is hindered by significant challenges, including the poor electrical conductivity of S and Li_2S, and the high solubility of Li polysulfides (LiPSs) in the electrolyte.[5,6]

Department of Chemical and Biological Engineering, Korea University, 145 Anam-ro, Seongbuk-gu, Seoul, 02841, Republic of Korea. E-mail: junhyukmoon@korea.ac.kr

† Electronic supplementary information (ESI) available. See DOI: https://doi.org/10.1039/d4ee02297a

‡ These authors contributed equally to this work.

In particular, LiPSs leaked into the electrolyte cause immediate loss of S, electrolyte depletion, and Li anode corrosion.[7–10] Recent efforts have effectively mitigated these problems by encapsulating S within conductive porous carbon substrates adorned with LiPS adsorptive and conversion-promoting metal compound electrocatalysts (*e.g.*, MgO,[11] Ti_4O_7,[12] $NiCoO_2$,[13] SnO_2,[14] VC,[15] CoP,[16] Co_9S_8,[17] Mo_2N,[18] Co_4N,[19] TiO_2,[20] MoO_3[21,22] and Nb_2O_5[23]). Such strategies have shown promise, especially under conditions of low S loading, achieving minimal capacity fade (0.034–0.112%) over 300–600 cycles, with initial discharge capacities ranging from 804 to 1053 mA h g^{-1} (Table S1, ESI†).

Despite these advancements, developing practical Li–S batteries with energy densities surpassing those of Li-ion batteries

9112 | *Energy Environ. Sci.*, 2024, **17**, 9112–9121

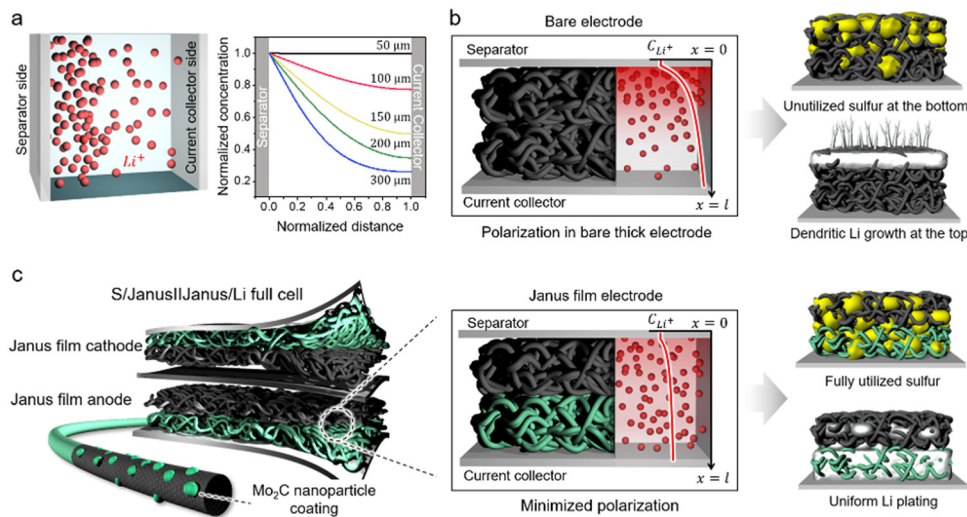This journal is © The Royal Society of Chemistry 2024

Fig. 1 Schematic illustrating the resolution of Li-ion polarization issues in a Janus electrode. (a) Li-ion polarization within a thick electrode, showing only Li-ions, with normalized ion concentration plotted against the normalized distance in the electrode ($x = 0$ represents the top surface, $x = 1$ the bottom). (b) Li-ion polarization in a thick host electrode (CNT film), leading to uneven S utilization at the cathode and Li top growth at the anode. (c) Structure of the Janus film full cell, improvement of Li-ion polarization in the Janus film, and resultant enhancement in electrode utilization at both the cathode and anode.

remains challenging, particularly due to the need for high S loading (>5 mg cm^{-2}) (Supplementary Note #1, ESI†).[24,25] A critical consideration for high S loading is the requirement for a cathode host substrate thickness >150–200 μm. This thickness introduces significant Li-ion polarization across the electrode, especially in porous carbon-based host substrates, impairing ion transport.[26,27] Using the Nernst-Planck equation, we describe ion transport dynamics influenced by both electric fields and concentration gradients.[26,27] Our results reveal significant Li-ion concentration gradients within host substrates with thicknesses ranging from 150 to 300 μm, compared to those at 50 μm (Fig. 1a). Specifically, Li-ion polarization—measured by the concentration differences at both ends of the substrate—reaches 50% at 150 μm and 74% at 300 μm (Supplementary Note #2, ESI†). This pronounced gradient leads to diffusion-limited charge–discharge at the cathode, causing uneven conversion across the electrode and significantly reducing overall sulfur utilization efficiency (Fig. 1b). Additionally, high sulfur loading demands rigorous control over Li anode reactions. To accommodate high-capacity cathode reactions, Li anodes experience substantial Li plating and stripping during charge/discharge cycles, accelerating dendritic Li growth and forming dead Li, which causes immediate capacity fading (Fig. 1b).[28,29] Thus, these challenges underscore the pressing need for an electrode architecture that comprehensively addresses both anodic and cathodic issues.

In this work, we demonstrate a Li–S cell incorporating a Janus architecture substrate for both the cathode and anode (Fig. 1c). The Janus substrate features a composition combining a bare carbon nanotube (CNT) or carbon fiber (CF) film with a Mo$_2$C nanoparticle-coated counterpart. This design markedly improves sulfur utilization across the entire cathodic film by regulating diffusion-limited reactions and substantially suppressing LiPS leakage—the "shuttle" effect (Fig. 1c).

Furthermore, the Janus film directs bottom-up growth of Li at the anode, achieving stable Li plating even under high-capacity conditions (Fig. 1c). Compared to the previous application of a carbon film uniformly coated with metal compound nanoparticles,[11-23] our Janus film with spatially modulated electrocatalyst coating achieves superior performance under practical sulfur loading conditions (Supplementary Note #3, ESI†). In the full cell configuration with Janus cathode/anode, we achieve a high discharge capacity of 1461 mA h g^{-1} and exceptional cycle stability with only 0.048% decay per cycle over 1000 cycles. Under practical conditions with an E/S ratio of 4.4 μL mg^{-1} and an N/P ratio of 2, we attain an energy density of 6.3 mA h cm^{-2}.

Preparation of Janus structure cathode and anode

The Janus cathode host is formed by bonding a Mo$_2$C-coated CNT film and a bare CNT film through a compressive calendering process. Mo$_2$C is widely recognized as a highly active electrocatalyst for water electrolysis and has been incorporated into Li–S cathode applications due to its strong affinity for LiPS.[30-32] The CNT film is produced by vacuum filtration of a CNT dispersion with a range of 10–200 nm (Fig. S1, ESI†). Mo$_2$C nanoparticles are obtained through thermal annealing using ammonium molybdate precursors. HRTEM confirms lattice fringes corresponding to the hexagonal Mo$_2$C (101) (Fig. S2, ESI†). The Raman spectrum of the Mo$_2$C-coated CNT films reveals a distinct peak at 822 and 995 cm^{-1}, characteristic of Mo$_2$C (Fig. S3, ESI†).[33] The Mo$_2$C-coated CNT films are obtained through a synthesis reaction of Mo$_2$C nanoparticles in the presence of CNT films (Fig. 2a). The size of the Mo$_2$C nanoparticles ranges from 30 to 50 nm (TEM/EDS, Fig. 2b). The coating content of Mo$_2$C is controlled at 20 wt% for the cathode
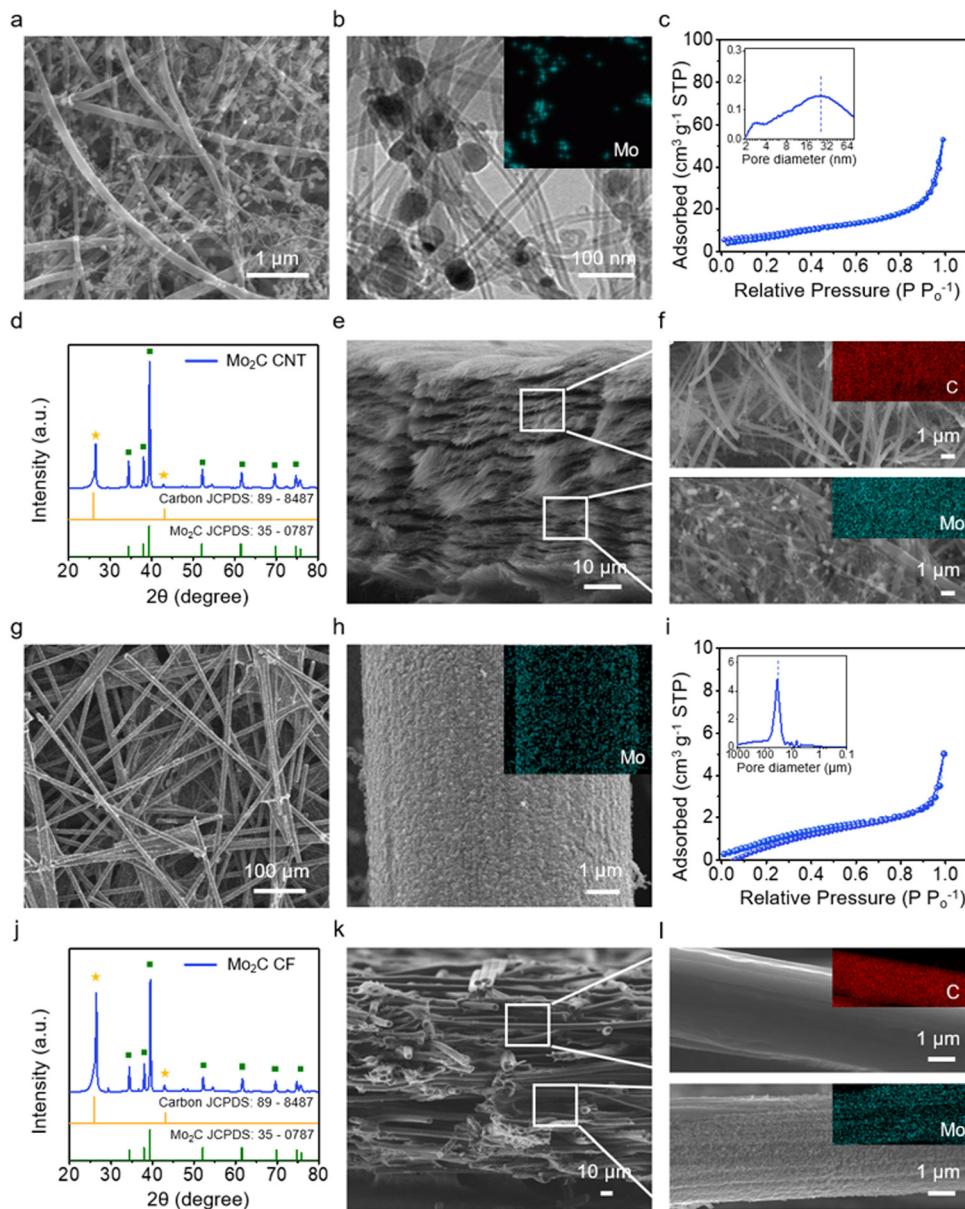
Fig. 2 Characterization of the Janus film host electrode. (a) SEM and (b) TEM/EDS mapping images of Mo$_2$C-CNT. (c) BET isotherm and pore size distribution (inset), and (d) XRD pattern of Mo$_2$C-CNT. (e) Cross-sectional SEM of the Janus cathode host (f) with magnified SEM and EDS mapping images of the top and bottom films. (g) SEM and (h) TEM/EDS mapping images of Mo$_2$C-CF. (i) BET isotherm and pore size distribution (inset), and (j) XRD pattern of Mo$_2$C-CF. (k) Cross-sectional SEM of the Janus anode host, (l) with magnified SEM and EDS mapping images of the top and bottom films.

(Fig. S4 and S5, ESI†). BET adsorption isotherm analysis confirms that the Mo$_2$C-coated CNT displays a specific surface area of 64 m^2 g^{-1}, with a predominant pore structure within the size range of 10 to 50 nm (Fig. 2c and inset).[34] The XRD pattern of the Janus film exhibits characteristic peaks at 34°, 38°, and 39°, corresponding to (100), (002), and (101) planes of hexagonal Mo$_2$C (Fig. 2d);[35] peaks with weaker intensities at 25° and 44° are attributed to CNT (Fig. 2d).[36] A cross-sectional SEM image of the Janus film is presented in Fig. 2e and f, with magnified SEM/EDS images for both the bare and Mo$_2$C-coated layers provided in Fig. S6 (ESI†). The cross-sectional and the magnified SEM images distinctly show a coating of Mo$_2$C on only one half of the film.

The Janus anode host is similarly formed by joining a Mo$_2$C-coated CF film with a bare CF film. CF films are chosen for their large pores, which accommodate high fluxes of Li, and have diameters of approximately 5 to 10 μm (SEM, Fig. 2g). The Mo$_2$C-coated CF film is fabricated in a manner similar to the cathode host. The coating content of Mo$_2$C is controlled at 20 wt% for the anode (Fig. S7 and S8, ESI†). The magnified surface images of CF show a uniform and high-density coating of Mo$_2$C nanoparticles (Fig. 2h). The Mo$_2$C-coated CF film features a pore structure with a size range of 30 to 50 μm (Fig. 2i and inset). The XRD pattern of the Mo$_2$C-coated CF film displays characteristic peaks for Mo$_2$C (Fig. 2j), with peaks at 26° and 43° attributed to CF,[37] corresponding to the graphite planes (002)

9114 | *Energy Environ. Sci.*, 2024, **17**, 9112–9121

This journal is © The Royal Society of Chemistry 2024

and (100), respectively. The cross-sectional images of the Janus anode film (Fig. 2k and l) clearly show a coating of Mo_2C on only one half of the film (Fig. S9, ESI†).

Inhibition of LiPS shuttle in the Janus cathode

We assess the adsorption efficiency of Mo_2C-CNT/CNT Janus film cathode substrates for LiPS. Upon immersion in a Li_2S_6 electrolyte, the Janus film demonstrated a faster rate of decolorization compared to the bare CNT film (Fig. 3a and inset). The adsorption capacity of the Janus film, as determined through UV-vis absorption of the electrolyte solution,[38] is confirmed to be approximately three times greater than that of the bare CNT film (Fig. S10, ESI†). This favorable adsorption of LiPS on Mo_2C nanoparticles is predicted by the binding energy from density functional theory (DFT) calculations (Fig. 3b).[39] The binding energies for Li_2S_6 and Li_2S_4 on the carbon surface are estimated at -0.55 eV and -0.62 eV, respectively, while on the Mo_2C surface, these energies are estimated at -2.08 eV and -1.31 eV. This comparison indicates that Mo_2C demonstrates a chemical affinity for LiPS that is approximately 2.4 times higher than that of the carbon surface

(Fig. S11–S13, ESI†). Supporting this observation, charge distribution analysis reveals significant electron delocalization upon the adsorption of LiPS on the Mo_2C surface (Fig. S14, ESI†).

The chemical interaction between LiPS and the Mo_2C substrate is elucidated by the Mo 3d XPS spectrum. Deconvolution of the spectrum for the Janus substrate reveals four doublet peaks. Doublet peaks at 228.2 eV and 231.4 eV are attributed to Mo^{2+}, while those at 229.1 eV and 232.8 eV are associated with the Mo oxycarbide phase.[40] In the spectrum of the Li_2S_6-adsorbed Janus substrate, the Mo^{2+} peak shifts to a lower binding energy by approximately -0.4 eV (Fig. 3c), suggesting electron transfer from the S to Mo, indicative of a chemical bond formation between Li_2S_6 and Mo_2C.[41] Additionally, the S 2p XPS analysis of the Mo_2C-coated substrate reveals a positive shift in binding energies corresponding to terminal sulfur at 162.7 eV and bridging sulfur at 163.9 eV.[42] This shift further confirms electron transfer between Mo_2C and LiPS, reinforcing the strong interaction between them (Fig. S15 and S16, ESI†).[43] Moreover, cyclic voltammetry analysis demonstrates the impact of Mo_2C on redox conversion, confirming that the Mo_2C substrate facilitates rapid kinetics during redox processes (Fig. S17, ESI†).

Now, we evaluate the leakage of LiPS over the course of charging/discharging on the Janus film cathode substrate.
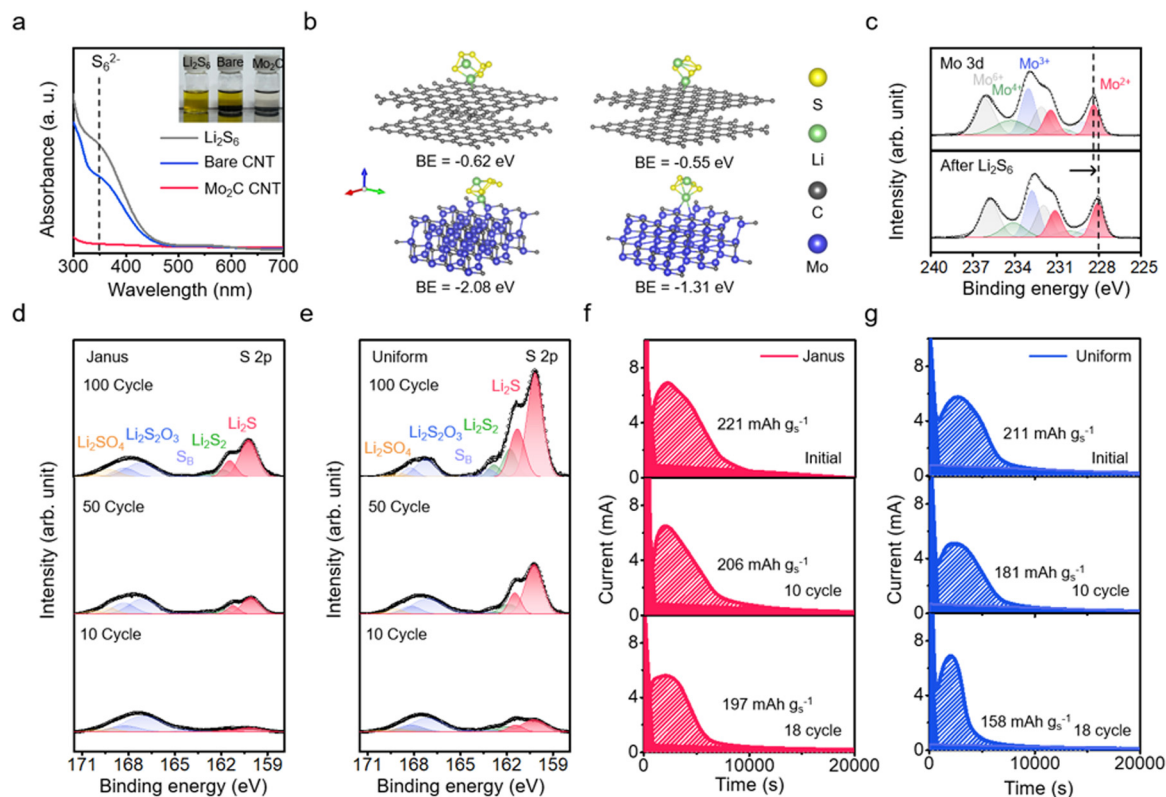

Fig. 3 Suppression of LiPS shuttle in the Janus film cathode. (a) UV-vis absorption spectra of bare and Mo_2C-CNT immersed Li_2S_6 electrolyte. The inset image shows the color change after adsorption. (b) Optimized adsorption configurations and binding energies on carbon and Mo_2C surfaces for Li_2S_6, and individually for Li_2S_4. (c) Mo 3d XPS spectra of the Mo_2C-CNT substrate before and after the adsorption of Li_2S_6. *Ex situ* XPS spectra of the Li metal anode (d) in Janus film cathode cells during charge/discharge cycles and (e) in uniform film cathode cells. Galvanostatic discharge profiles for the LiPS–Li_2S conversion during charge/discharge cycles in (f) Janus film cathode cells and (g) in uniform film cathode cells.

This journal is © The Royal Society of Chemistry 2024

Energy Environ. Sci., 2024, **17**, 9112–9121 | **9115**

This analysis involves monitoring the formation of Li$_2$S$_2$/Li$_2$S at the Li anode, a direct result of LiPS shuttling, using S 2p XPS analysis. Specifically, we compare the extent of Li$_2$S/Li$_2$S$_2$ formation among the Janus substrate, a bare CNT film substrate, and a CNT film substrate uniformly coated with Mo$_2$C nanoparticles (uniform Mo$_2$C-CNT film). The S 2p spectrum displays peaks at 161.8 eV and 160.2 eV, corresponding to Li$_2$S$_2$ and Li$_2$S, respectively (Fig. 3d and e and Fig. S18, ESI†).[42] Peaks at 170.2 eV and 167.2 eV are assigned to Li$_2$SO$_4$ and Li$_2$SO$_3$, respectively; these species indicate the formation of the SEI layer from LiTFSI salt.[44,45] The Janus substrate exhibits significantly suppressed Li$_2$S$_2$/Li$_2$S peaks compared to the bare CNT film.[46] Notably, the Janus film shows lower peak intensities compared to the uniform Mo$_2$C-CNT film. In measurements of shuttle current, the Janus film exhibits a significantly lower shuttle current than not only the bare CNT film but also the uniform Mo$_2$C-CNT film (Fig. S19, ESI†).[47] This suggests that shuttle suppression is a fundamental characteristic of the structure of the Janus film, likely resulting from the slowed diffusion of lithium polysulfide (LiPS), which primarily forms in the Mo$_2$C-coated CNT bottom layer; the diffusion is obstructed by the bare CNT top layer before it crosses the separator. This is corroborated by comparing the primary deposition sites of Li$_2$S using *ex situ* SEM and measuring the interfacial resistance from *operando* EIS analysis on both the Janus and uniform films, as a function of the depth of discharge (DoD) (Fig. S20 and S21, ESI†).

To assess whether the diffusion of LiPS is confined within the CNT film layer, we estimate the diffusion length (L) of LiPS. This length is defined by the diffusion coefficient (D) and time (t) as:

$$L = \left(\sqrt{6Dt} \right)$$

The D in a porous film is derived from $D = D_{bulk}\, \varepsilon/\tau$, with D_{bulk} representing the bulk diffusivity, and τ and ε denoting the tortuosity and porosity, respectively. With a given D_{bulk} for LiPS of 2.6×10^{-13} m^2 s^{-1}, and τ and ε values of 1.1 and 0.5 for the CNT film,[48–50] and considering the charge/discharge duration at $1C$, we calculate L to be approximately 40 μm. Indeed, the corresponding length is sufficiently small compared to the thickness of the bare CNT film, confirming that the shuttle of LiPS across the separator can be effectively suppressed by the bare CNT film.

We evaluate the potentiostatic discharge capacity of the Janus film cathode cell, which is composed of a Li metal anode and a cathode loaded with 5 mg cm^{-2} of S (Fig. 3f and g and Fig. S22, ESI†). The discharge profile is characterized by an initial plunge in current, followed by a peak indicative of Li$_2$S nuclei growth, and a gradual decrease in current, suggesting the coalescence of these nuclei.[51] From the area under the current–time (i–t) curve, we can calculate the discharge capacity, which represents the capacity for the conversion from LiPSs to Li$_2$S.[52] The Janus film cathode achieves a capacity retention of approximately 89% by the 18th cycle. In comparison, the uniform Mo$_2$C-CNT film shows a capacity retention of around 75% after 18 cycles. During cycling, the Janus film cathode maintains relatively high capacity retention, which further supports the effective suppression of the LiPS shuttle.

Stable Li plating/stripping with the Janus film anode

We employ a Mo$_2$C-CF/CF Janus film as the anode host substrate. First, we compare the galvanostatic profiles of the Janus film anode with those of the bare CF film anode and the CF film anode uniformly coated with Mo$_2$C (uniform Mo$_2$C-CF film) (Fig. 4a and Fig. S23, ESI†). We choose CF films for their larger pores and superior conductivity, which are favorable for lithium plating/stripping.[53] These measurements are conducted in half cells, using Li foil as a counter electrode, at a current density of 1 mA cm^{-2} and a capacity of 10 mA h cm^{-2}. The Janus film achieves a low overpotential of 10 mV, comparable to that of the uniform Mo$_2$C-CF film and approximately 50% less than that of the bare CF film (Fig. 4a). This result suggests that Mo$_2$C facilitates Li nucleation.[54] Our DFT calculations reveal that the binding energy of Li on Mo$_2$C is −2.55 eV, significantly higher than the binding energy of −1.29 eV for Li on the carbon surface (Fig. 4b and c), confirming that Mo$_2$C serves as an active site for Li nucleation, lowering the energy barrier for Li plating. *Ex situ* SEM analysis during Li plating exhibits the preferential nucleation on Mo$_2$C particles (Fig. S24, ESI†).

Further, we evaluate the Coulombic efficiency of Li plating/stripping cycles for these anode substrates (Fig. 4d). Remarkably, the Janus film maintains stable performance, achieving a Coulombic efficiency of 99.9% after 100 cycles. The bare CF film displays fluctuating Coulombic efficiency from the beginning, leading to the cessation of measurements around 30 cycles. The uniform Mo$_2$C-CF film, while showing stable cycling, experiences a significant decrease in the efficiency, dropping to 85% at 100 cycles. This comparison highlights the critical influence of not only the presence of Mo$_2$C but also its spatial distribution within the CF film. We directly observe the growth morphology of Li in these host substrates following Li plating (Fig. 4e–h). On the bare CF film, a "top growth" morphology is evident, characterized by the predominant deposition of Li on the top layer of the film (Fig. S25, ESI†). This top growth indicates that Li plating in the CF film is diffusion-limited;[55] that is, the limited diffusion into the interior prevents the porous structure from adequately accommodating the Li plating (Fig. S26, ESI†). It is noteworthy that the uniform Mo$_2$C-CF film exhibits a similar top growth morphology to the bare CF film; this is evidenced by the silver–grey coloration on the upper part of the film, indicative of metallic Li (Fig. 4e and f). Contrary to the Li plating observed on the top, the porous interior of the film exhibits significantly less Li deposition. In contrast, the Janus film achieves uniform deposition of Li throughout the CF film, effectively preventing Li accumulation at the top (Fig. 4g and h); the digital camera
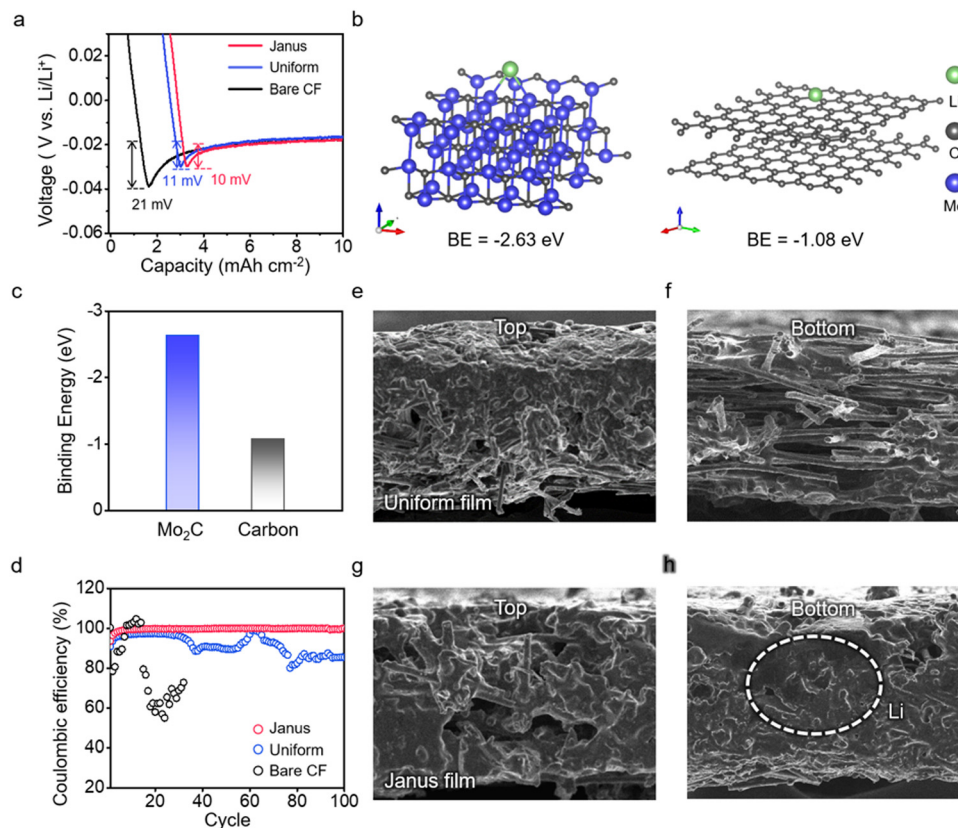
9116 | *Energy Environ. Sci.*, 2024, **17**, 9112–9121

This journal is © The Royal Society of Chemistry 2024

Fig. 4 Li plating on Janus film anode substrates. (a) Voltage profiles of Janus film, uniform Mo$_2$C-CF film, and bare CF film substrates during Li plating. (b) Optimized atomic configurations for Li adsorption on Mo$_2$C and carbon surfaces, and (c) corresponding binding energies. (d) Coulombic efficiencies of Janus film, uniform Mo$_2$C-CF film, and bare CF film anode substrates during Li plating/stripping cycles at 1 mA cm^{-2} and 1 mA h cm^{-2}. Cross-sectional SEM images of the top and bottom of both (e) and (f) uniform Mo$_2$C-CF film and (g) and (h) Janus film after Li plating at 10 mA h cm^{-2}.

image of the Janus film remains black, signifying minimal top growth (Fig. S27 and S28, ESI†). This comparison indicates that at high capacities and current densities, where Li plating is significantly diffusion-limited,[56] controlling reaction kinetics from a macroscopic perspective is essential in a porous anode host (Supplementary Note #4, ESI†).

We assess the long-term cycling stability of Li plating/stripping under varied current densities. We compare the performance of Janus film anodes with that of the uniform Mo$_2$C-CF film anodes and the Li foil anodes (Fig. S29 and S30, ESI†). At a current density of 5 mA cm^{-2}, the Li foil anodes show significant instability, with overpotential necking occurring after just 14 cycles (Fig. 5a). The voltage profile is marked by a pronounced concave shape, indicative of severe solid–electrolyte interphase (SEI) breakage and uncontrolled dendrite growth (Fig. 5b).[57,58] The uniform Mo$_2$C-CF film anodes experience unstable voltage fluctuations and cease cycling after 80 cycles. This behavior corresponds with the observed increase in top-growth during cycling, as shown in Fig. 4e. In contrast, the Janus film anodes exhibit stable cycling up to 100 cycles (equivalent to 200 hours), achieving the lowest overpotential among the anodes. This exceptional stability is attributed to the internal accommodation of Li growth, as observed in Fig. 4h. EIS measurements further corroborate this stable Li plating/stripping, demonstrating that the charge transfer resistance at

the anode surface remains consistent throughout the cycling (Fig. S31, ESI†). Even at elevated current densities of 10 mA cm^{-2}, the Janus film anode demonstrates remarkable stability over 100 cycles (200 hours), without any voltage fluctuations (Fig. 5c). The enlarged voltage profile displays a smooth contour without any overpotential features (Fig. 5d). In contrast, both the uniform anode and the Li foil anode exhibit significantly reduced cycle stability. Notably, the stability of the uniform film anode decreases further compared to its performance at 5 mA cm^{-2}.

Furthermore, we investigate the cycling performance of Janus film anodes at ultra-high capacities of 20 mA h cm^{-2}, a capacity necessary to accommodate that of a S-loaded cathode at 10 mg cm^{-2} (Fig. 5e). Remarkably, the Janus film sustains a stable profile for up to 200 cycles (2000 hours). The uniform Mo$_2$C-CF film anode and the Li foil anode show significant overpotential from the start and fail after 92 and 23 cycles, respectively. The voltage hysteresis (overpotential during Li stripping/plating) over cycles of the Janus film anode shows stable maintenance up to 200 cycles, in contrast to the uniform Mo$_2$C-CF film anode and the Li foil anode (Fig. 5f). These findings indicate that regulated Li plating in the Janus structure plays a crucial role in achieving stable cycling, particularly under conditions of high capacity and current density.

To further evaluate the robustness of the Janus film anodes, we conducted a time-control test to determine the critical current
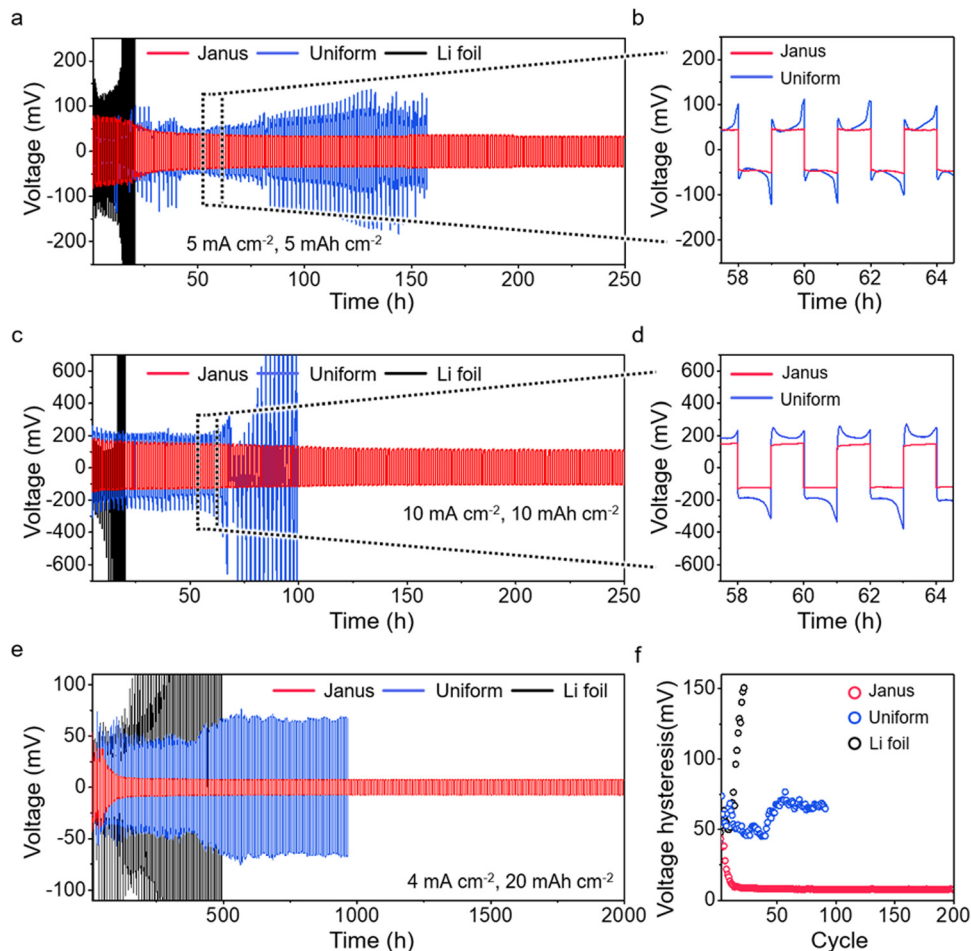
Fig. 5 Li plating/stripping cycling of Janus film anode symmetric cells. Galvanostatic cycling profiles and voltage hysteresis of symmetrical cells using Janus film, uniform Mo_2C-CF film, and Li foil anodes at (a) a current density of 5 mA cm^{-2} with an areal capacity of 5 mA h cm^{-2}, (c) a current density of 10 mA cm^{-2} with an areal capacity of 10 mA h cm^{-2}, and (e) a current density of 4 mA cm^{-2} with an areal capacity of 20 mA h cm^{-2}. (b) and (d) Magnified profiles of (a) and (c), respectively. (f) Voltage hysteresis over cycles for Janus film, uniform Mo_2C-CF film, and Li foil anode.

density.[59] The test revealed that the critical current density of the Janus electrode reached 15.0 mA cm^{-2}, demonstrating its ability to accommodate higher current densities (Fig. S32, ESI†).

Performance of the Li–S full cell

We prepare a Li–S full cell incorporating a Janus film as both anode and cathode hosts, referred to as the S/Janus‖Janus/Li full cell. For comparison, we also prepare a cell with a Janus film cathode and a Li metal anode (S/Janus‖Li cell), and a cell with a CNT film cathode and a Li metal anode (the S/CNT‖Janus/Li cell). The discharge/charge profiles of these cells are presented in Fig. 6a; all cells are prepared with a S loading of 1 mg cm^{-2} on the cathode, with an S content is 62.5 wt%, and Li plating on the anode for a N/P ratio of 10. The S/Janus‖Janus/Li full cell deliver the highest discharge capacity, reaching 1461 mA h g^{-1}. In comparison, the discharge capacities for the S/Janus‖Li cells and the S/CNT‖Janus/Li cells are 1414 mA h g^{-1} and 1116 mA h g^{-1}, respectively. Moreover, the voltage polarization between the charge and discharge plateaus of the

S/Janus‖Janus/Li full cell is observed to be lower (174 mV) compared to the S/Janus‖Li cells (187 mV) and the S/CNT‖Janus/Li cells (276 mV) (Fig. 6b). This reduced polarization in the S/Janus‖Janus/Li full cells can be primarily attributed to the lower potential barrier at the charging plateau, which is a result of stable Li plating on the Janus film anode. These comparisons highlight the synergy in the S/Janus‖Janus/Li full cells between the suppression of the LiPS shuttle at the Janus cathode and the stable Li growth at the Janus anode. The rate performance of these cells is evaluated across a current range from 0.2 C to 4 C (Fig. 6c and Fig. S33, ESI†). The cells exhibit an impressive capacity retention of 75.2% with a 20-fold increase in C-rate, surpassing the S/Janus‖Li cells and S/CNT‖Janus/Li cells, which maintain 69.8% and 64.8% capacity retention, respectively. The superior rate capability of the S/Janus‖Janus/Li full cells is also evident in their charge transfer resistance, measured *via* EIS at high C-rates, demonstrating lower resistance by 19.9% and 62.6% respectively compared to the S/Janus‖Li cell and the S/CNT‖Janus/Li cell (Fig. S34, ESI†).

Long-term cycling stability of these cells is assessed at a 1 C (Fig. 6d and Fig. S35, ESI†). The S/CNT‖Janus/Li cell exhibits

9118 | *Energy Environ. Sci.*, 2024, **17**, 9112–9121

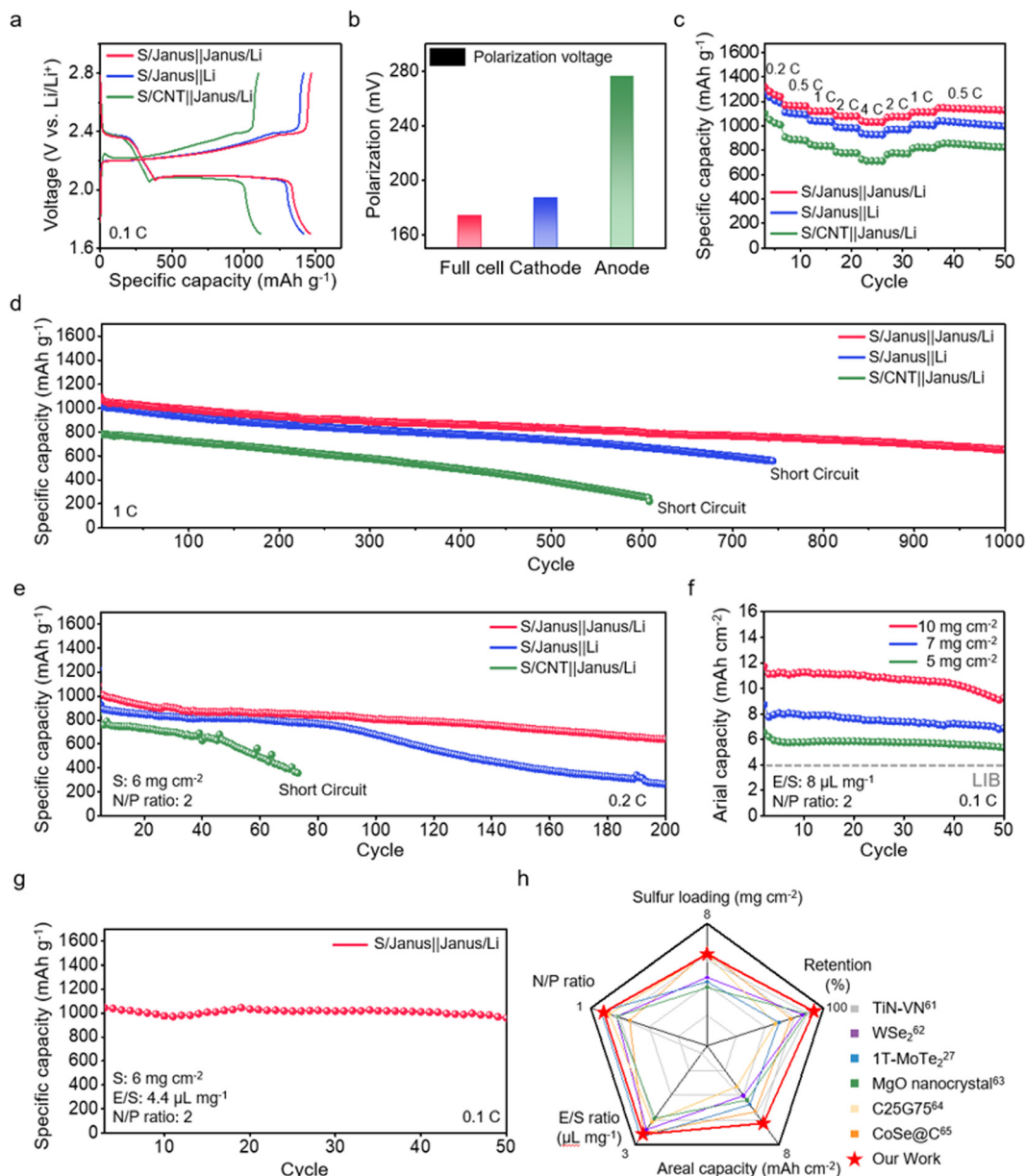This journal is © The Royal Society of Chemistry 2024

Fig. 6 Performance of Li–S full cells. (a) Galvanostatic charge–discharge profiles, (b) voltage polarization, (c) specific capacities at various C-rates, and (d) long-term cycling. (e) Specific capacities under high S loading for cells with different configurations: Janus cathode‖Janus anode, Janus cathode‖Li metal, and CNT cathode‖Janus anode. (f) Areal capacities of the Janus cathode‖Janus anode full cell under ultra-high S loading. Under practical conditions with a S loading of 6 mg cm^{-2}, an E/S ratio of 4.4 μL mg^{-1}, and an N/P ratio of 2, (g) performance of the Janus cathode‖Janus anode full cell, and (h) comparison with other studies.

rapid capacity fade, retaining only 48.8% of its initial capacity after 500 cycles; this degradation may be primarily due to the pronounced LiPS shuttle observed within the bare CNT cathode. The S/Janus‖Li cell maintains a capacity retention of 72.5% up to 744 cycles before experiencing a short circuit; SEM images of the Li anode after cycling reveal significant dendritic growth on the surface, potentially leading to cell performance degradation (Fig. S36, ESI†). The S/Janus‖Janus/Li full cell demonstrates the highest long-term stability, preserving 78.1% of its initial capacity after 500 cycles and showing a minimal decay rate of 0.048% across 1000 cycles.

Under high loading and low N/P conditions, we conduct long-term cycling tests on each cell at a rate of 0.2 C (Fig. 6e and Fig. S37, ESI†). The S/Janus‖Janus/Li full cell shows a high initial capacity of 1013 mA h g^{-1}, with a decay rate of 0.228% per cycle. This rate is significantly more stable, being three times lower than the 0.625% decay rate per cycle of the S/Janus‖Li cell. The S/CNT‖Janus/Li cells exhibit an unstable cycling profile from the beginning and eventually short circuit at 73 cycles. The S/Janus‖Janus/Li full cell, operating under a condition of N/P = 2, achieves exceptional capacities at high S loadings of 5 mg cm^{-2} and 7 mg cm^{-2}—6.5 mA h cm^{-2} and

This journal is © The Royal Society of Chemistry 2024

Energy Environ. Sci., 2024, **17**, 9112–9121 | **9119**

8.7 mA h cm^{-2}, respectively—and also attains a high areal capacity of 11.7 mA h cm^{-2}, even at an ultra-high S loading of 10 mg cm^{-2}. Such performance not only significantly surpasses the areal capacity of 4 mA h cm^{-2} typical in conventional Li-ion batteries but also exceeds achievements reported in prior studies (Fig. 6f and Fig. S38 and S39 and Table S2, ESI†). Under practical conditions with a S loading of 6 mg cm^{-2}, an E/S ratio of 4.4 μL mg^{-1}, and an N/P ratio of 2, the full cell displays a capacity of 1044 mA h g^{-1} (areal capacity 6.3 mA h cm^{-2}) and maintains 91.7% capacity retention after 50 cycles (Fig. 6g). A comparison of this performance with that of the dual functional host full cells in prior studies is presented in Fig. 6h and Table S3 (ESI†).[60–65] Notably, the S/Janus‖Janus/Li full cell demonstrates superior cycle life and retention, even under high S loading conditions.

Conclusion

This study presents Janus film host substrates, engineered to manage high S loadings essential for achieving high energy densities in Li–S batteries. The innovative heterogeneous Janus structure, featuring layers of Mo$_2$C-coated and uncoated CNTs or CFs, tackles both cathodic and anodic issues common in traditional Li–S battery systems. Utilizing the adsorptive capacity of Mo$_2$C nanoparticles for LiPS and the diffusion delay provided by the uncoated CNT layer, the Janus cathode substrate significantly reduces the shuttle effect and boosts S utilization. Simultaneously, the Janus anode substrate mitigates diffusion-limited Li growth, facilitating Li plating/stripping within the porous CF layer and thereby enhancing Coulombic efficiency even at extremely high current densities. The application of Janus films as both anode and cathode in full cells culminates in exceptional electrochemical performance, especially at high S loadings. Such Janus full cells achieve the highest recorded discharge capacity of 1461 mA h g^{-1}. Furthermore, a Janus full cell maintains a high capacity retention rate of 75% after a C-rate increase of 20-fold, alongside remarkable long-term cycling stability, evidenced by a capacity decay rate of just 0.048% over 1000 cycles. At an ultra-high S loading of 10 mg cm^{-2}, a Janus full cell delivers an initial areal capacity of 11.7 mA h cm^{-2}. Our research provides insights suggesting that strategic approaches must be explored, not only at the microscopic level, such as introducing electrocatalysts for the host substrate, but also at the macroscopic level, by regulating uniform sulfur and lithium reaction kinetics within the host electrode.

Author contributions

Kyungsik Um: formal analysis; investigation; methodology; software. Chanho Jung: data curation; formal analysis. Hyunsuk Nam: formal analysis. Haeli Lee: formal analysis. Saegi Yeom: formal analysis. Jun Hyuk Moon: conceptualization; funding acquisition; project administration; supervision; writing – original draft; writing – review & editing.

Data availability

The data supporting the findings of this study are available within the article and its ESI.† Additional data, including raw datasets and analysis scripts, are available from the corresponding author upon reasonable request.

Conflicts of interest

The authors declare no conflicts of interest.

Acknowledgements

References

1 P. G. Bruce, S. A. Freunberger, L. J. Hardwick and J.-M. Tarascon, *Nat. Mater.*, 2012, **11**, 19–29.

2 B. Scrosati, J. Hassoun and Y.-K. Sun, *Energy Environ. Sci.*, 2011, **4**, 3287–3295.

3 W. Guo, W. Zhang, Y. Si, D. Wang, Y. Fu and A. Manthiram, *Nat. Commun.*, 2021, **12**, 3031.

4 L. Huang, T. Lu, G. Xu, X. Zhang, Z. Jiang, Z. Zhang, Y. Wang, P. Han, G. Cui and L. Chen, *Joule*, 2022, **6**, 906–922.

5 L. Fan, M. Li, X. Li, W. Xiao, Z. Chen and J. Lu, *Joule*, 2019, **3**, 361–386.

6 A. Manthiram, S. H. Chung and C. Zu, *Adv. Mater.*, 2015, **27**, 1980–2006.

7 J.-Q. Huang, Q. Zhang, H.-J. Peng, X.-Y. Liu, W.-Z. Qian and F. Wei, *Energy Environ. Sci.*, 2014, **7**, 347–353.

8 R. Liu, Z. Wei, L. Peng, L. Zhang, A. Zohar, R. Schoeppner, P. Wang, C. Wan, D. Zhu and H. Liu, *Nature*, 2024, **626**, 98–104.

9 H. Kim, G. Jeong, Y.-U. Kim, J.-H. Kim, C.-M. Park and H.-J. Sohn, *Chem. Soc. Rev.*, 2013, **42**, 9011–9034.

10 Y. Liu, Y. Elias, J. Meng, D. Aurbach, R. Zou, D. Xia and Q. Pang, *Joule*, 2021, **5**, 2323–2364.

11 X. Tao, J. Wang, C. Liu, H. Wang, H. Yao, G. Zheng, Z. W. Seh, Q. Cai, W. Li and G. Zhou, *Nat. Commun.*, 2016, **7**, 11203.

12 Q. Pang, D. Kundu, M. Cuisinier and L. Nazar, *Nat. Commun.*, 2014, **5**, 4759.

13 Y. T. Liu, D. D. Han, L. Wang, G. R. Li, S. Liu and X. P. Gao, *Adv. Energy Mater.*, 2019, **9**, 1803477.

14 Y. Yao, C. Chang, R. Li, D. Guo, Z. Liu, X. Pu and J. Zhai, *Chem. Eng. J.*, 2022, **431**, 134033.

15 J. Zheng, C. Guan, H. Li, Y. Xie, S. Li, J. Hu, K. Zhang, B. Hong, Y. Lai and J. Li, *Chem. Eng. J.*, 2022, **442**, 135940.

9120 | *Energy Environ. Sci.*, 2024, **17**, 9112–9121

This journal is © The Royal Society of Chemistry 2024

16 R. Sun, Y. Bai, Z. Bai, L. Peng, M. Luo, M. Qu, Y. Gao, Z. Wang, W. Sun and K. Sun, *Adv. Energy Mater.*, 2022, **12**, 2102739.

17 P. Zeng, X. Zhou, J. Peng, X. Huang, B. Chang, G. Chen, M. Chen, L. Zheng, Y. Pei and J. Su, *Adv. Funct. Mater.*, 2023, **33**, 2211818.

18 M. Yang, P. Liu, Z. Qu, F. Sun, Y. Tian, X. Ye, X. Wang, X. Liu and H. Li, *Nano Energy*, 2022, **104**, 107922.

19 Z. Sun, S. Vijay, H. H. Heenen, A. Y. S. Eng, W. Tu, Y. Zhao, S. W. Koh, P. Gao, Z. W. Seh and K. Chan, *Adv. Energy Mater.*, 2020, **10**, 1904010.

20 D. Gueon, J. Yoon, J. Cho and J. H. Moon, *Adv. Sci.*, 2022, **9**, 2200958.

21 D. Gueon, T. Kim, J. Lee and J. H. Moon, *Nano Energy*, 2022, **95**, 106980.

22 H. Lee, H. Nam and J. H. Moon, *Energy Storage Mater.*, 2024, 103551.

23 S. Yeom, H. Jo, H. Lee and J. H. Moon, *Energy Storage Mater.*, 2024, 103644.

24 A. Bhargav, J. He, A. Gupta and A. Manthiram, *Joule*, 2020, **4**, 285–291.

25 G. Zhou, H. Chen and Y. Cui, *Nat. Energy*, 2022, **7**, 312–319.

26 Y. Kuang, C. Chen, D. Kirsch and L. Hu, *Adv. Energy Mater.*, 2019, **9**, 1901457.

27 X. Zhang, Z. Ju, Y. Zhu, K. J. Takeuchi, E. S. Takeuchi, A. C. Marschilok and G. Yu, *Adv. Energy Mater.*, 2021, **11**, 2000808.

28 M. Wang, Z. Bai, T. Yang, C. Nie, X. Xu, Y. Wang, J. Yang, S. Dou and N. Wang, *Adv. Energy Mater.*, 2022, **12**, 2201585.

29 W. Xu, J. Wang, F. Ding, X. Chen, E. Nasybulin, Y. Zhang and J.-G. Zhang, *Energy Environ. Sci.*, 2014, **7**, 513–537.

30 J. Wan, J. Wu, X. Gao, T. Li, Z. Hu, H. Yu and L. Huang, *Adv. Funct. Mater.*, 2017, **27**, 1703933.

31 Y. Huang, Q. Gong, X. Song, K. Feng, K. Nie, F. Zhao, Y. Wang, M. Zeng, J. Zhong and Y. Li, *ACS Nano*, 2016, **10**, 11337–11343.

32 S. Niu, S.-W. Zhang, R. Shi, J. Wang, W. Wang, X. Chen, Z. Zhang, J. Miao, A. Amini and Y. Zhao, *Energy Storage Mater.*, 2020, **33**, 73–81.

33 Z. Liu, J. Li, S. Xue, S. Zhou, K. Qu, Y. Li and W. Cai, *J. Energy Chem.*, 2020, **47**, 317–323.

34 K. Kim, J. Kim and J. H. Moon, *Adv. Sci.*, 2023, **10**, 2206057.

35 C. Li, Z. Wang, M. Liu, E. Wang, B. Wang, L. Xu, K. Jiang, S. Fan, Y. Sun and J. Li, *Nat. Commun.*, 2022, **13**, 3338.

36 D. Zhang, L. Shi, J. Fang, X. Li and K. Dai, *Mater. Lett.*, 2005, **59**, 4044–4047.

37 L. Dobiášová, V. Starý, P. Glogar and V. Valvoda, *Carbon*, 1999, **37**, 421–425.

38 Y. Yang and J. Zhang, *Adv. Energy Mater.*, 2018, **8**, 1801778.

39 B. Yu, A. Huang, D. Chen, K. Srinivas, X. Zhang, X. Wang, B. Wang, F. Ma, C. Liu and W. Zhang, *Small*, 2021, **17**, 2100460.

40 S. Zhu, C. Wang, H. Shou, P. Zhang, P. Wan, X. Guo, Z. Yu, W. Wang, S. Chen and W. Chu, *Adv. Mater.*, 2022, **34**, 2108809.

41 X. Liang, A. Garsuch and L. F. Nazar, *Angew. Chem.*, 2015, **127**, 3979–3983.

42 X. Liang, C. Hart, Q. Pang, A. Garsuch, T. Weiss and L. F. Nazar, *Nat. Commun.*, 2015, **6**, 5682.

43 R. Wang, J. Yang, X. Chen, Y. Zhao, W. Zhao, G. Qian, S. Li, Y. Xiao, H. Chen and Y. Ye, *Adv. Energy Mater.*, 2020, **10**, 1903550.

44 V. Etacheri, R. Marom, R. Elazari, G. Salitra and D. Aurbach, *Energy Environ. Sci.*, 2011, **4**, 3243–3262.

45 W. Li, H. Yao, K. Yan, G. Zheng, Z. Liang, Y.-M. Chiang and Y. Cui, *Nat. Commun.*, 2015, **6**, 7436.

46 M. T. Lee, H. Liu and D. Brandell, *Batteries Supercaps*, 2020, **3**, 1370–1376.

47 C. Y. Chen, H. J. Peng, T. Z. Hou, P. Y. Zhai, B. Q. Li, C. Tang, W. Zhu, J. Q. Huang and Q. Zhang, *Adv. Mater.*, 2017, **29**, 1606802.

48 T. Zhang, M. Marinescu, S. Walus and G. J. Offer, *Electrochim. Acta*, 2016, **219**, 502–508.

49 B. J. Hinds, N. Chopra, T. Rantell, R. Andrews, V. Gavalas and L. G. Bachas, *Science*, 2004, **303**, 62–65.

50 B. Natarajan, I. Y. Stein, N. Lachman, N. Yamamoto, D. S. Jacobs, R. Sharma, J. A. Liddle and B. L. Wardle, *Nanoscale*, 2019, **11**, 16327–16335.

51 F. Y. Fan, W. C. Carter and Y.-M. Chiang, *Adv. Mater.*, 2015, **27**, 5203–5209.

52 Z. Ye, Y. Jiang, L. Li, F. Wu and R. Chen, *Adv. Mater.*, 2020, **32**, 2002168.

53 T. T. Zuo, X. W. Wu, C. P. Yang, Y. X. Yin, H. Ye, N. W. Li and Y. G. Guo, *Adv. Mater.*, 2017, **29**, 1700389.

54 J. Cao, Y. Xie, Y. Yang, X. Wang, W. Li, Q. Zhang, S. Ma, S. Cheng and B. Lu, *Adv. Sci.*, 2022, **9**, 2104689.

55 W. Liu, D. Lin, A. Pei and Y. Cui, *J. Am. Chem. Soc.*, 2016, **138**, 15443–15450.

56 J. Yun, B.-K. Park, E.-S. Won, S. H. Choi, H. C. Kang, J. H. Kim, M.-S. Park and J.-W. Lee, *ACS Energy Lett.*, 2020, **5**, 3108–3114.

57 C.-J. Huang, B. Thirumalraj, H.-C. Tao, K. N. Shitaw, H. Sutiono, T. T. Hagos, T. T. Beyene, L.-M. Kuo, C.-C. Wang and S.-H. Wu, *Nat. Commun.*, 2021, **12**, 1452.

58 J. Seo, W. Jeong, M. Lim, B. Choi, S. Park, Y. Jo, J. W. Lee and H. Lee, *Energy Storage Mater.*, 2023, **60**, 102827.

59 Y. Lu, C. Z. Zhao, H. Yuan, X. B. Cheng, J. Q. Huang and Q. Zhang, *Adv. Funct. Mater.*, 2021, **31**, 2009925.

60 J. He, A. Bhargav and A. Manthiram, *Adv. Energy Mater.*, 2022, **12**, 2103204.

61 Y. Yao, H. Wang, H. Yang, S. Zeng, R. Xu, F. Liu, P. Shi, Y. Feng, K. Wang and W. Yang, *Adv. Mater.*, 2020, **32**, 1905658.

62 P. Wang, F. Sun, S. Xiong, Z. Zhang, B. Duan, C. Zhang, J. Feng and B. Xi, *Angew. Chem.*, 2022, **61**, e202116048.

63 P. Wang, B. Xi, Z. Zhang, N. Song, W. Chen, J. Feng and S. Xiong, *Small*, 2021, **17**, 2103744.

64 G. T. Yu and S. H. Chung, *Small*, 2023, **19**, 2303490.

65 J. He and A. Manthiram, *Adv. Energy Mater.*, 2020, **10**, 52002654.

This journal is © The Royal Society of Chemistry 2024

Energy Environ. Sci., 2024, **17**, 9112–9121 | 9121